Citation for published version:
Rhead, A, Butler, R, Liu, W, Kim, BC & Hallett, S 2013, 'Compression after impact strength of a buckling resistant, tow steered panel'.

Publication date:
2013

Document Version
Early version, also known as pre-print

Link to publication

University of Bath

COMPRESSION AFTER IMPACT STRENGTH OF A BUCKLING RESISTANT, TOW STEERED PANEL

A.T. Rhead[1]*, R. Butler[1], W. Liu[1], B.C. Kim[2] and S.R. Hallett[2]
[1] Composites Research Unit, University of Bath, Bath, UK,
[2] Advanced Composites Centre for Innovation and Science, University of Bristol, Bristol, UK
* Corresponding author (A.T.Rhead@bath.ac.uk)

Keywords: *Compression after impact, tow-steering, damage tolerance*

Abstract

A novel form of fiber steering (Continuous Tow Shearing (CTS)) which eliminates manufacturing defects found in other steered fiber techniques, e.g. tow-overlaps, tow gaps and tow wrinkling, has recently been developed. By using CTS to steer fibers in-plane, structures with improved buckling capacity can be achieved leading to lower mass designs. Such optimal designs for minimum mass CTS laminates have been produced using the infinite strip program VICONOPT. The resulting distribution of fiber orientation and mass across the width of these optimized laminates results in regions of high stress near supports. These regions, which are vital to the integrity of the CTS laminate, are at risk of reduction in compressive strength caused by Barely Visible Impact Damage (BVID). Hence, using experimental tests combined with a unique analytical approach, the paper explores the effect of near support impact damage on the compressive strength of CTS panels. Results indicate a failure strain that matches industrial straight fiber alternatives but that is below the design failure strain. Hence there is scope for further optimization of CTS laminates for improved damage tolerance.

1 Introduction

Emissions targets and increasing fuel costs are driving aircraft manufacturers to seek ever lighter structures. Indeed to meet the stringent targets set out in documents such as ACARE 2050 a significant step change in both composite performance and manufacturing capability is a necessity. By steering fibers to tailor stiffness and better distribute loading across a structure, Advanced Fiber Placement (AFP) manufacturing techniques are generating significant theoretical buckling performance increases over straight fiber designs [1]. However, practical gains are restricted by the limited radius of curvature (635mm for a 3.175mm tow width or 1778mm for a 6.35mm tow width) [2] that can be achieved before process induced defects such as inner tow wrinkling become apparent [3]. By shearing fiber tows at the point of application, Continuous Tow Shearing (CTS), allows much tighter radii of curvature (up to 30mm for a 7mm tow width) [4] to be achieved without the occurrence of process defects. The significantly improved steering capability of CTS allows weight reductions of up to 35% in comparison to optimized straight fiber designs [5] without loss in buckling capacity; a key design driver for aerospace structures.

While weight reductions offered by CTS are highly encouraging, the issue of Barely Visible Impact Damage (BVID) has not yet been considered. BVID has been shown to reduce straight fiber laminate strength by up to 60% from its pristine value. The mechanism that causes this is often buckling of surface plies, delaminated during impact, driving further growth of delaminations and ultimately causing failure [6]. In this paper, a steered fiber CTS laminate has been optimized, using the infinite strip optimization program VICONOPT [7], to achieve a realistic buckling load with minimum mass. Two panels have been manufactured based on this design and this paper reports the first results on their response to impact and Compression After Impact (CAI) testing. A unique analytical Strip model [6] for assessing CAI strength of straight fiber laminates, assuming buckling-driven propagation, is used to analyze the damage tolerance of the optimized CTS laminates. In a companion paper [8] the Strip model is incorporated into a minimum mass optimization procedure.

2 Minimum mass CTS panel

An optimization routine developed in [5] which employs the VICONOPT infinite strip method [7] is

used to optimize a CTS panel with stacking sequence $[+\theta/-\theta/-\varphi/+\varphi]_S$ (where θ and φ vary across the panel width, see Fig. 1). Optimization minimizes mass subject to buckling and CTS manufacturing constraints [4]. Boundary conditions and panel dimensions for the optimization are given in Fig. 1. Panel dimensions were chosen to allow the use of supports conditions similar to those in ASTM standard D7137 [9] during experimental CAI testing. The material properties E_{11} = 163 GPa, E_{22} = 6.8 GPa, G_{12} = 3.4 GPa, ν_{12} = 0.28, G_{1C} = 200 J/m^2 and ρ = 1584 kg/m^3 were assumed.

A half panel comprising ten unique 5mm strips was optimized in the VICONOPT model. The full panel being produced by mirroring strips about the mid-line of the panel, see Fig. 1(a). In each unique strip the fiber angle is free to vary (within CTS radius of curvature constraints) resulting in a prismatic structure with fiber angle varying across the width of the panel. A sensitivity study on the number of strips was conducted in [5]. Steering of CTS fiber tows results in a fiber angle dependent increase in tow thickness from t_0 (unsheared) to t_θ (sheared) where,

$$t_\theta = \frac{t_0}{\sin \theta} \qquad (1)$$

Table 1 gives the fiber angles θ and φ and associated lamina thicknesses t_θ and t_φ for each unique VICONOPT strip in the optimized design. During the manufacturing process interpolation across the strips is used to produce a design with continuous fiber paths, see Fig. 1(a).

By steering from low stiffness fibers in the center of the panel to high stiffness fibers at the edge, the optimized design redistributes load from the center of the panel to regions near the boundary that would typically be supported by stiffeners, see Fig. 1. Angle dependent thickening of tows also redistributes stress to the edge of the panel further alleviating stress in the center and increasing buckling capacity.

The resulting optimized design buckles at 85kN (ε_x = 6783 microstrain). The optimized panel offers a theoretical weight saving of 34% in comparison with a straight fiber laminate with ply thickness 0.15mm and optimized stacking sequence $[45/-45/0_2/-45/45/0_2/90/0]_S$ where optimization was for the same support conditions and buckling constraints.
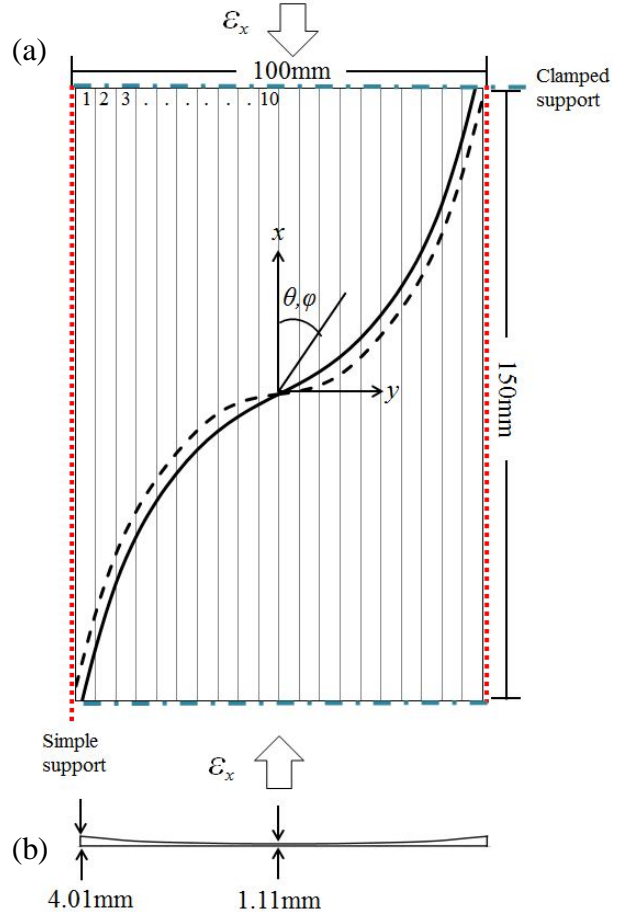

Fig. 1 Optimized CTS steered laminate showing (a) fiber angle distributions for θ (solid curve) and φ (dashed curve) and (b) thickness distribution across the width. Sides are simply-supported and loading edges clamped. Load is applied as axial strain ε_x. Strip numbers in the top left corner correspond to Table 1.

Table. 1 Optimized CTS steered laminate fiber angle (θ and φ) and lamina thickness (t_θ and t_φ) for VICONOPT discrete optimized design. Strip numbers relate to Fig. 1.

Strip no.	1	2	3	4	5	6	7	8	9	10
θ (deg.)	15.6	18.2	23.5	30.0	35.9	41.4	47.6	54.2	59.4	62.7
t_θ (mm)	0.48	0.42	0.33	0.26	0.22	0.20	0.18	0.16	0.15	0.15
φ (deg.)	14.5	18.4	25.2	32.1	37.7	42.8	50.6	62.5	74.0	80.7
t_φ (mm)	0.52	0.41	0.31	0.24	0.21	0.19	0.17	0.15	0.14	0.13

3 Test methods

The following section provides details of experimental methods for the impact and CAI testing of two CTS panels which are based on the optimized design of Section 2.

3.1 Test panel design

The CTS test panels (see Fig. 2) are an extended version of the panel described in Fig. 1. As noted in Section 2 the stiff outer regions of the optimized panel are highly stressed and integral to the panel's strength. The steep fiber angles in these regions are also intolerant to damage [6]. This combination makes the outer edges of the design critical for damage and hence a near edge location is chosen for impact. However, impact too close to the panel edge may lead to premature interaction of damage with edge effects and supports both during impact and compression loading. In order to avoid this, test panels were manufactured with an additional half panel. Two CTS panels were manufactured from 7mm wide (in the unsheared state) carbon fiber reinforced plastic (CFRP) tape [4]. Material properties are the same as those in Section 2. The extended panel has a VICONOPT buckling load of 194kN at ε_x = 6587 microstrain.

The CTS process results in one flat laminate face (against the tool) and a concave face with varying thickness, see Fig. 2(a). Note that the thickness variation builds throughout the laminate during lay-up and does not only exist on the surface. This results in an uneven distribution of material about the laminate mid-plane. Following cure this uneven distribution produces a small curvature across the width of the laminate. Central deformation of the curvature is toward the flat surface which becomes slightly convex. In order to ensure level surfaces for contact with vertical supports in the CAI tests, additional 10mm wide constant fiber angle regions were included in the panel manufacture as shown on Fig. 1(a). Similarly, horizontal edges were potted in resin to ensure a flat contact at the clamped supports.

3.2 Impact

A preliminary impact study indicated that an impact energy of 8J produced a suitable level of impact damage. Impact was delivered to the non-flat surface of the panels by an Instron Dynatup 9250 HV instrumented impact test machine employing a
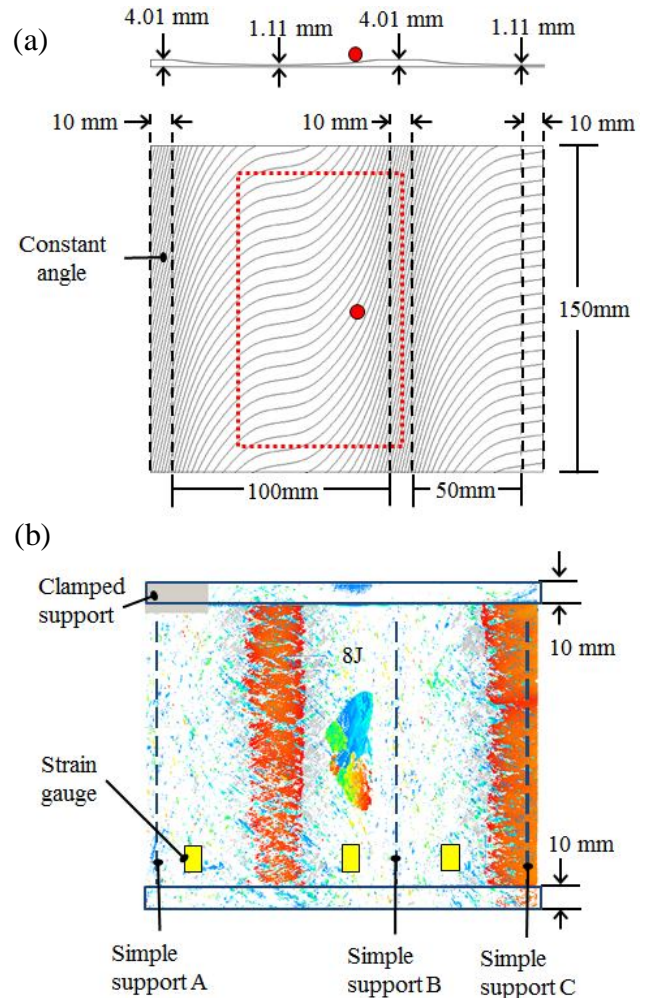

Fig. 2 (a) Cross-sectional thickness distribution, impact window (broken boundary) and panel dimensions. The impact point is shown with a dot. (b) Ultrasonic C-scan of Panel 2 showing impact damage and positions of CAI test fixture supports and strain gauges.

16mm hemispherical tup. During impact, panels were clamped over an 75 x 125mm ASTM D7136 [10] impact window. As shown in Fig. 2 the long window edge was aligned with the position of the central simple support that would be used in the CAI fixture (Fig. 3). This provides consistency in support conditions across the impact and CAI tests. In order to avoid supports interfering with the formation of damage, impact was delivered away from the edge of the window. Following impact, C-scan images of the damage were taken using an Ultrasonic Sciences Ltd. C-scan system and a Nikon XT225H X-Ray Computed Tomography (XRCT) system.

3.3 Compression after impact

A modified CAI fixture based on the ASTM D7137 standard test fixture [9] was used to hold the panels during compression testing, see Fig. 3.
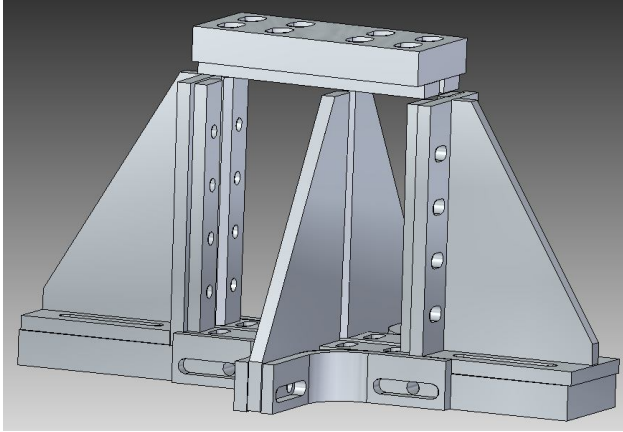

Fig. 3 CAI test fixture. ε_x is applied vertically. The three vertical simple supports and two horizontal clamped supports match those shown in Fig. 2.

The ASTM CAI window is maintained in one half of the fixture, see the left hand side of Figs. 2 and 3. In a departure from ASTM D7137 top and bottom supports were clamped rather than guided to prevent edge brooming failures. Note that the cure-induced curvature of the panel is restrained along its horizontal edge when it is placed in the clamped supports. Support positions in relation to the fiber distribution and impact location can be seen in Fig. 2. Compressive displacement was applied to the two panels at a rate of 0.1mm/min using an Instron 5585H electric test machine. Vertical in-plane strains were monitored throughout all tests by pairs of back-to-back strain gauges placed on areas of equal thickness, see Fig. 2. Out-of-plane displacement and axial strain of the flat (non-impact) face, relative to an unloaded reference state, was also captured throughout by a Limess Digital Image Correlation (DIC) system employing a stereo pair of Photron SA3 cameras. Testing of Panel 2 was interrupted following audible cracking and both an XRCT-scan and a C-scan were performed before the specimen was reloaded and tested to failure.

4 Results

4.1 Impact

Impacts to both panels produced damage that was essentially identical in delamination size and morphology. As can be seen from the C-scan image in Fig. 4(a), overall delamination size was considerably larger than might be expected; an 8J impact to a straight fiber laminate would typically be entirely contained within a 40mm diameter circle. Colors in Fig. 4 indicate depth from the non-impact surface. Note that the transition of colors within individual delaminations indicates a variation in depth and hence sublaminate thickness. Post impact XRCT scans (Fig. 4(c)) demonstrate that the damage morphology has the usual 'spiral staircase' pattern of interconnected delaminations and interplay cracks. The only exception being that one half of the delaminations that would normally form in a symmetrical 'peanut shaped' pair have extended toward the stiffened boundary and the steeper fibers in this area, see Figs. 2(b) and 4(a). As impact occurred on the non-smooth surface of the panels, dent depths were difficult to determine but were certainly shallower than the industrial threshold depth (0.3mm) for BVID. However, visual and XRCT inspection identified surface cracking on both surfaces following impact, see Fig. 5. This suggests that damage may actually be classified as clearly visible despite the dent depth. Such cracks followed the edges of near surface delaminations.

4.2 Compression after impact

Both panels were tested to failure. However, Panel 1 failed when the central simple support on the impact face side gave way following full panel buckling. Hence, any analysis of this panel is limited to loads well below the failure load. Both panels exhibited sublaminate buckling prior to failure as was captured on the DIC system, see Fig. 6. Based on delamination orientation and vertical position, a comparison of Figs. 2(b), 4 and 6 indicates that sublaminate buckling occurred above a delamination at the first interface. From the outset of loading, out-of-plane deflection of the panel in the same direction as the sublaminate buckle and initial panel curvature (toward the flat face) occurred. This deflection continued to grow until failure. Figure 7 shows a comparison of average strain gauge readings versus load for all three tests on Panels 1 and 2.

(a)

Length: 34mm
(1st interface)

Length: 35.6mm
(3rd interface)

Impact point (impact
on opposite face)

(b)

D

C

A

A

B

B

D

C

ε_x

ε_x Center
support

(c)

No
damage

1 ply

2 plies

3 plies

1 ply

1 ply

1 ply

3 plies

3 plies

1 ply

1 ply

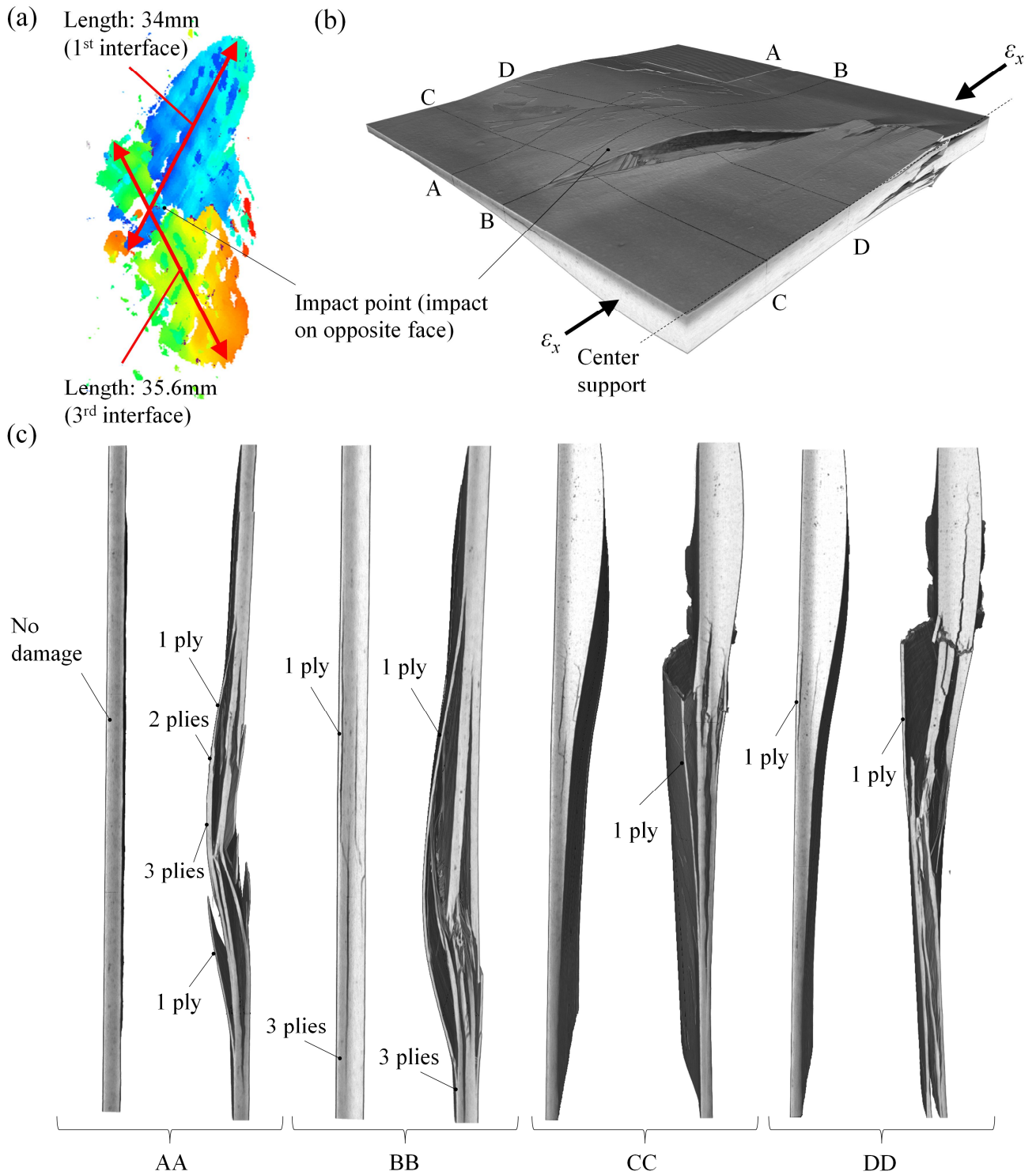1 ply

1 ply

AA

BB

CC

DD

Fig. 4 (a) C-scan of damage in Panel 2 prior to CAI testing. (b) XRCT scan of Panel 2 showing damage extent following failure. (c) Cross-sections at locations AA, BB, CC and DD through (b); left hand images are following impact and right hand images following failure. Non-smooth rectangular areas on the surface of the 3D view are artifacts of the visualization process.
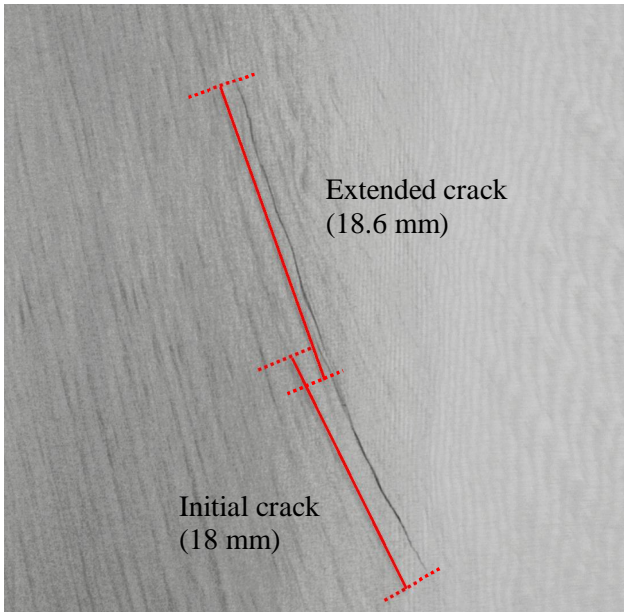
Fig. 5 XRCT scan of impact surface showing extent of crack growth following the first loading of Panel 2.

The theoretical VICONOPT load-strain line is also shown. Figure 8 shows the strain gauge output versus load plot for Panel 2 during its first loading. Gauges 3 and 4 (see Figs. 2(c) and 8) were located in line with the damage and hence the lower strains recorded by this pair of gauges are expected. A change in stiffness of these gauges at approximately 35-40kN corresponds with detection of sublaminate buckling on the DIC images (37kN). Divergence in strain gauge output between 70 and 85kN and the re-stiffening that follows are a consequence of full panel buckling being prevented by the central simple supports. From 90kN onward, kinks in strain gauge traces in Fig. 8 are characteristic of damage events and were accompanied by cracking sounds. The first loading of Panel 2 was halted at 126kN following significant cracking sounds. XRCT scans taken when the test was halted indicate that an existing surface crack on the impact face had extended toward the central simple support, see Fig. 5. The crack had also joined with delaminations close to the non-impact face, creating a crack running through almost the entire thickness of the panel. However, in-line with DIC data, preliminary interrogation of ultrasonic C scans and XRCT scans taken when testing of Panel 2 was halted revealed no obvious sign of delamination growth, i.e. the surface crack extension does not appear to be linked to delamination growth. Following the scans on Panel 2 it was reloaded until failure occurred. The failure loaded reached (122kN) was slightly below the previous peak load (126kN).
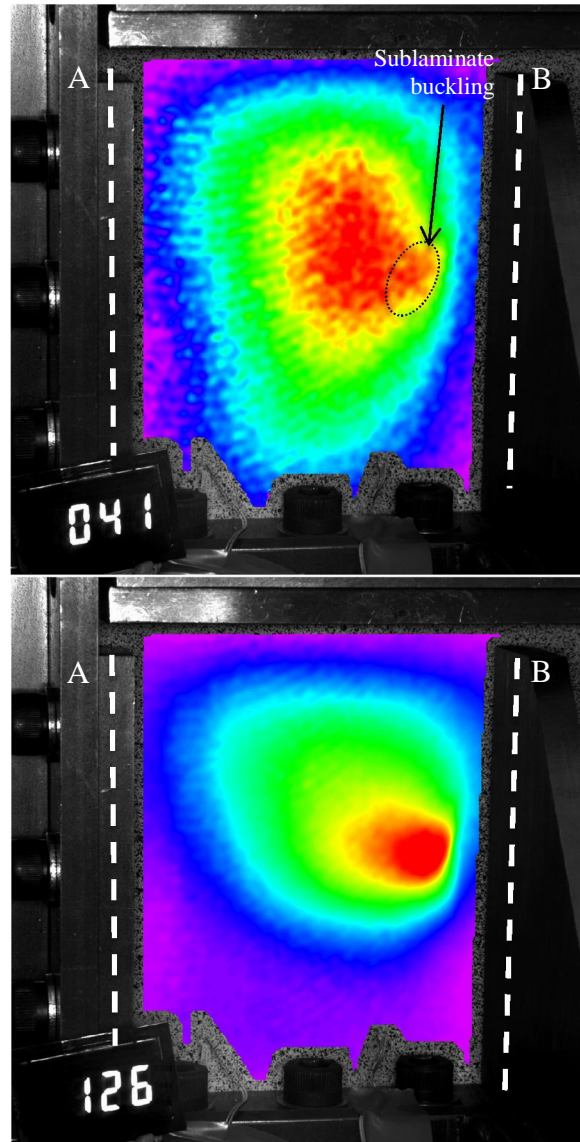

Fig. 6 DIC images of impacted area of Panel 2 (a) showing the early stages of sublaminate buckling and bending deformation, (b) immediately prior to the first loading being halted. Central areas (red) are closer to the reader. The LED screen displays the compressive load in kN. Broken lines are approximate positions of simple supports from Fig. 2(b).

Although the mechanism for failure was indeterminate, there was visible evidence of edge and sublaminate buckling-driven failures.
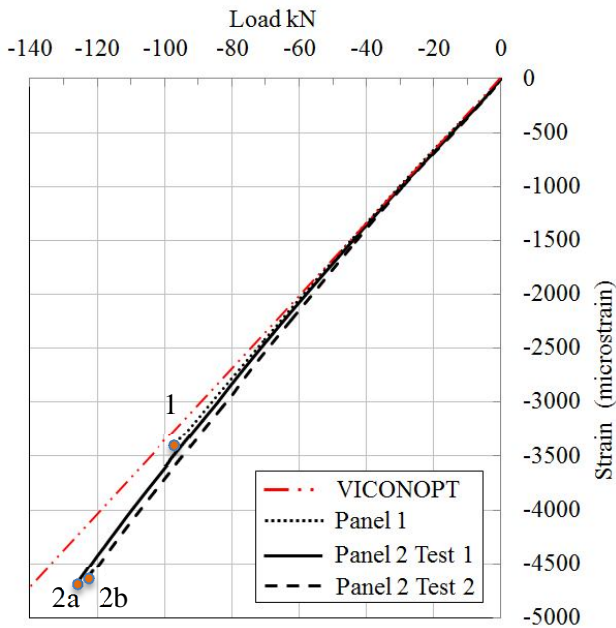
Fig. 7 Load vs. average strain gauge readings for Panel 1 and both Panel 2 test runs. Theoretical VICONOPT stiffness is also shown. End of test load: 1 at 95kN, 2a at 126kN and 2b at 122kN.

Figure 4 shows XRCT images of Panel 2 following failure with cross-sections near the impact point. Sublaminate buckling and delamination growth is evident at the 1st and 3rd ply interfaces from the top (non-impact) surface. Delaminations are also seen to bridge multiple depths i.e. cross-section AA in Fig. 4(b) shows a buckled sublaminate made up of a

varying number of plies. However, whether delamination growth caused failure or was instead caused by another failure event remains unclear.

5 Strip model for CAI analysis of CTS laminates

A unique Strip model for calculation of the threshold strain ε_{th}, below which sublaminate buckling-driven delamination propagation will not occur in a straight fiber laminate, has previously been presented [6]. As a precursor to application to laminates with steered fibers, straight fiber laminates artificially delaminated to produce various $[\pm\theta]$ sublaminate configurations have been tested and analyzed [11]. Here a brief overview of the Strip model is provided together with the assumptions required to employ it in the analysis of CTS laminates. In the following subscript L is used for laminate variables where laminate refers to the full laminate. Similarly, SL is used for sublaminate variables. Sublaminate refers to a thin stack of one or more plies, separated by delamination but which remain connected to the laminate along the perimeter of the delamination.

5.1 Strip model for straight fiber laminates

The Strip model assumes that delaminations resulting from impact damage (intraply cracking is ignored) can be approximated by a circle containing the full extent of each individual delamination. It is also assumed that each of these circles can be considered in isolation from the others, i.e. the
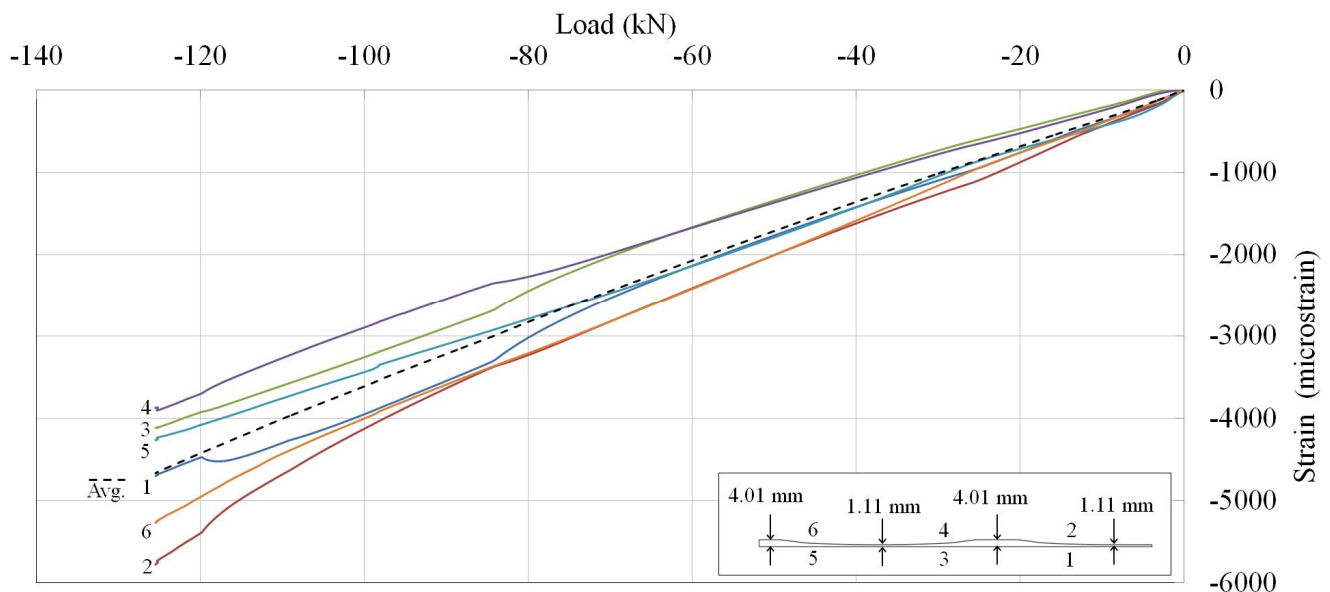

Fig. 8 Load vs. strain gauge readings for Panel 2 test 1. The inset shows strain gauge locations, also see Fig. 2(c).

material around the delamination is assumed to be pristine. Loading of sublaminates is via an axial compressive strain ε_x applied to the laminate and a transverse strain ε_y resulting from the Poisson's ratio of the laminate. For a fully coupled sublaminate,

$$
\begin{Bmatrix} N_x \\ N_y \\ N_{xy} \\ M_x \\ M_y \\ M_{xy} \end{Bmatrix}_{SL} = \begin{bmatrix} A_{11} & A_{12} & A_{13} & B_{11} & B_{12} & B_{13} \\ A_{21} & A_{22} & A_{23} & B_{21} & B_{22} & B_{23} \\ A_{31} & A_{32} & A_{33} & B_{31} & B_{32} & B_{33} \\ B_{11} & B_{12} & B_{13} & D_{11} & D_{12} & D_{13} \\ B_{21} & B_{22} & B_{23} & D_{21} & D_{22} & D_{23} \\ B_{31} & B_{32} & B_{33} & D_{31} & D_{32} & D_{33} \end{bmatrix}_{SL} \begin{Bmatrix} \varepsilon_x \\ \varepsilon_y \\ 0 \\ 0 \\ 0 \\ 0 \end{Bmatrix}_L \quad (2)
$$

The left hand vector gives the loads/moments acting on the sublaminate as a result of the laminate strains. It is assumed that the overall laminate is symmetric and balanced and hence is uncoupled and has no curvature. Compatibility with the laminate ensures that the sublaminate also has zero curvature. The in-plane sublaminate loading (i.e. sublaminate coupling effects producing moments are ignored) is input into the infinite strip program VICONOPT where a transcendental eigenvalue problem is solved to produce buckling modes and values of sublaminate buckling strain [12]. The lowest strain is taken as the critical sublaminate buckling strain ε^C. Once sublaminate buckling strains have been established for all delaminations, ε_{th} can be calculated,

$$
\varepsilon_{th} = \varepsilon^C \left(\sqrt{4 + \frac{2G_{IC}}{A_{11}(\varepsilon^C)^2}} - 1 \right) \quad (3)
$$

Here A_{11} is the axial stiffness of the sublaminate parallel to the loading axis and G_{IC} is the strain energy release rate required to cause mode I fracture of the resin. The delamination/sublaminate with the lowest value of ε_{th} is the threshold strain for the laminate.

5.2 Application to CTS laminates

An analysis of the location of impact damage in Fig. 2(b) indicates that the extent of the damage is contained almost entirely within a 15mm wide band. Comparison with Table 1 and Figure 1 indicates that this band coincides with strips 3, 4 and 5 in Table 1. Hence, as a first approximation, the average of the fiber angles and lamina thicknesses of these strips is

used to establish an equivalent straight fiber problem. The resulting straight fiber problem has stacking sequence $[+29.8/-29.8/-31.7/+31.7]_S$ and lamina thicknesses $t_\theta = 0.270$ mm and $t_\varphi = 0.253$ mm respectively. Strip model results are given in Table 2. Diameters for the assumed circular delaminations are given by the measurements in Fig. 4. Note that the 2nd interface will not delaminate as plies 2 and 3 have essentially parallel fibres.

Table. 2 Strip model and local experimental microstrain results for buckling (ε^C) and propagation (ε_{th}) at the 1st and 3rd interfaces. The experimental propagation strain ε_{th} is the local strain at failure.

Interface		1	3
ε^C	Strip model	826	3451
	Experimental	960	-
ε_{th}	Strip model	3428	3828
	Experimental	3960	

6 Discussion

6.1 Impact damage

Impact size and morphology were found to be repeatable suggesting a consistency of manufacturing quality was achieved. The unexpectedly large extent of delamination (probably a consequence of the relatively low fracture toughness of the matrix) suggests that damage resistance for this particular CTS design may need improving. However, this is somewhat offset by the extent of surface cracking (also linked to low fracture toughness) which makes impact damage more visible. The implication being that a lower energy impact and thus area of damage will be correlated with BVID. The proximity of the support to the impact point and the unequal distribution of thickness across the impact window, producing a more flexible area away from the impact, is thought to account for the elongated shape of some delaminations. The cure-induced curvature of the laminate will also have contributed to this effect. In this case, the laminate curvature means impact is on a concave face and hence a softened response would occur. However, impact to the flat surface would occur on a convex face resulting in a stiffer response and larger damage area. Thus the CTS panel may have a preferential direction for impact. A comparison can be drawn with impact on curved shells. The asymmetric nature of the panel means that impact on the flat face of the panel should be

considered before final conclusions are made about the damage resistance of the panel. The non-smooth surface of the impact face means that ultrasonic inspection of damage may not be possible in-service.

6.2 Compression after impact

Sublaminate buckling above the first interface was detected on the DIC system at approximately 37kN. As shown in Fig. 5 the sublaminate buckle formed on a convex surface. This Convexity increased with increasing ε_x and thus the local strain around the delaminated area became increasingly divergent from the average of the 6 strain gauges, i.e. the far-field strain. Hence, the average of the strain gauges (960 microstrain) in line with the damage is used to approximate the local strain at sublaminate buckling. Table 2 shows the Strip model result for sublaminate buckling above the first interface is conservative and within 14% of the experimental value.

Cracking sounds and growth of a crack on the impact face of the laminate were noted during the tests on Panel 2. However, it is not clear what, if any, effect this had on the failure of the panels. No delamination propagation was detected prior to failure. However, failure was sudden and hence delamination growth could have occurred and led to immediate failure. This would not have been captured by the DIC system which was capturing one image per second during the tests. Additionally, a post-test XRCT inspection (Fig. 4) of Panel 2 indicates that both edge stresses [14] and (buckling-driven) delamination propagation on the non-impact face may have played a role in the failure. For instance, Figs. 4(b) and (c) show significant 1st and 3rd ply delamination growth below buckled sublaminates, although growth is also seen at other interfaces. Buckled sublaminates with regions that are 1, 2 and 3 plies thick are visible on Fig. 4(c), indicating crack jumping between interfaces has occurred. Sublaminate buckling-driven delamination growth or an alternative failure mechanism may have occurred on the unmonitored impact surface.

The lower strain around the buckled sublaminate implies that less energy than is suggested by the far-field strain will be available to cause delamination propagation [15]. With this in mind, at failure, the average of the pair of strain gauges in-line with damage was 3960 microstrain. Similar values were captured in the vicinity of the edge of the buckled sublaminate by the DIC system. Strip model results

for growth at the 1st and 3rd interfaces are conservative and within 14% and 4% respectively of this local experimental value, see Table 2. Although there is both experimental and analytical evidence for a sublaminate buckling-driven failure it is not clear whether this mechanism drove or was driven by other failure events. However, irrespective of the failure mechanism, the damage tolerant strains suggested by the Strip model were indicative of the panel strength and as such provide a basis for optimisation for damage tolerance of other CTS panels. The far-field strain at failure of Panel 2 was 4670 microstrain which is comparable with a typical damage tolerant strain allowable for an aerospace composite panel but below the design strain of 6587 microstrain. Hence, there is a necessity to incorporate damage tolerance into the optimization procedures in Section 2. This is undertaken within a companion paper [8].

7 Conclusions and future work

The infinite strip program VICONOPT was used to optimize a CTS panel for minimum mass and a buckling load constraint. A theoretical 34% reduction in mass was achieved in comparison to an optimized straight fiber design. Two panels, based on this design, were manufactured using a Continuous Tow Shearing (CTS) technique. Preliminary impact tests and analysis using a unique Strip model identified highly stressed near-support locations as likely to show poor damage resistance and critical damage tolerance. In subsequent compression after impact testing, failure occurred at an axial strain of approximately 4700 microstrain; a strain comparable with current damage tolerant strain allowables. However, the design strain of 6587 microstrain was not reached and thus the panels cannot be considered damage tolerant to this level of strain. The mechanism for failure was difficult to ascertain as evidence for sublaminate buckling-driven delamination growth, intraply cracking and edge failure were present on XRCT scans. The cure-induced curvature of the panel meant that the sublaminate buckling occurred on a convex face. This lowered local compression strains around the buckled sublaminate and hence increased the applied strain at which delamination propagation would occur. However, an analysis based on sublaminate buckling driven failure using a unique Strip model delamination propagation strain

predictions were conservative and within 14% for 1st interface propagation and 4% for 3rd interface propagation of the local strain captured by DIC and strain gauges at failure. A companion paper [8] takes advantage of this accuracy by integrating the optimization of CTS panels with the Strip model and produces a much improved damage tolerant design with a minimum weight penalty.

Impact to the opposite face of the panels, owing to the through-thickness asymmetry of the panel and the resulting cure induced curvature, would produce a stiffer response to impact, leading to a larger damage area. Additionally, in this case, sublaminate buckling would occur on a concave face thereby increasing local compression (in comparison to the applied strain) and thus the likelihood of premature failure. Hence the damage tolerance of the panel requires further investigation.

Acknowledgements

References

[1] Z. Gürdal, B.F. Tatting and C.K. Wu "Variable stiffness composite panels: Effects of stiffness variation on the in-plane and buckling response". *Compos Part A: Appl. Sci. Manuf.*, Vol. 39, No.5, pp. 911-922, 2008.

[2] A.W. Blom "Structural performance of fiber-placed variable-stiffness composite conical and cylindrical shells". *PhD Thesis*, University of Delft, Holland, 2010.

[3] A. Beakou, M. Cano, J.-B. Le Cam and V. Verney "Modelling slit tape buckling during automated prepreg manufacturing: A local approach". *Comp. Struct.*, Vol. 93, pp. 2628-2635, 2011.

[4] B.C. Kim, K. Potter and P.M. Weaver "Continuous tow shearing for manufacturing variable angle tow composites". *Compos Part A: Appl. Sci. Manuf.*, Vol. 43, pp. 1347-1356, 2012.

[5] W. Liu, and R. Butler "Buckling Optimization of Variable Angle Tow Panels Using The Infinite Strip Method". *AIAA J.,* 2013. doi: 10.2514/1.J052123.

[6] R. Butler, A.T. Rhead, W. Liu and N. Kontis "Compressive strength of delaminated aerospace Composites". *Phil. Trans. Roy. Soc. A*, Vol. 370, pp. 1759-1779, 2012.

[7] F.W. Williams, D. Kennedy, R. Butler and M.S. Anderson "VICONOPT: program for exact vibration and buckling analysis or design of prismatic plate assemblies". *AIAA J.*, Vol. 29, pp. 1927–1928, 1991.

[8] W. Liu, R. Butler and A.T. Rhead "Optimised fiber steering and layer stacking for elastically tailored, damage tolerant laminates". *The 19th International Conference on Composite Materials,* Montreal, Canada, 2012.

[9] ASTM International, "Standard test method for compressive residual strength properties of damaged polymer matrix composite plates," ASTM D7137/D 7137M-07, 2007.

[10] ASTM International "Test Method for Measuring the Damage Resistance of a Fiber-Reinforced Polymer Matrix Composite to a Drop-Weight Impact Event" ASTM D7136/D 7136M-12, 2012.

[11] A.T. Rhead, R. Butler, W. Liu and N. Baker, "The influence of surface ply fibre angle on the compressive strength of composite laminates containing delamination". *The Aeronautical Journal*, Vol. 116, No. 1186, pp. 1315-1330. 2012.

[12] W.H. Wittrick and F.W. Williams "Buckling and vibration of anisotropic or isotropic plate assemblies under combined loadings". *Int. J. Mech. Sci.,* Vol. 16, pp.209–239. 1973.

[13] A.T. Rhead, R. Butler, and G.W. Hunt "Post-buckled propagation model for compressive fatigue of impact damaged laminates". *Int. J. Sol. Struct.* Vol. 45, pp. 4349-4361, 2008.

[14] K. Kaczmarek, M.R. Wisnom, M.I. Jones "Edge delamination in curved $(0_4/\pm45_6)_s$ glass-fibre/epoxy beams loaded in bending". *Comp. Sci. Tech.,* Vol. 58, No. 1, pp. 155-161.

[15] A.T. Rhead, R. Butler, and G.W. Hunt "Compressive Strength Following Delamination Induced Interaction of Panel and Sublaminate Buckling". *Proceedings of the 53rd AIAA, ASME, ASCE, AHS, and ASC Structures, Structural Dynamics, and Materials Conference*, Waikiki, Hawaii, April 2012.